Draft version October 23, 2007
Preprint typeset using LaTeX style emulateapj v. 03/07/07

SLAC-PUB-12919
October 2007

HOW VERY MASSIVE METAL FREE STARS START COSMOLOGICAL REIONIZATION

John H. Wise[1,2] and Tom Abel[1]

Draft version October 23, 2007

ABSTRACT

The initial conditions and relevant physics for the formation of the earliest galaxies are well specified in the concordance cosmology. Using ab initio cosmological Eulerian adaptive mesh refinement radiation hydrodynamical calculations, we discuss how very massive stars start the process of cosmological reionization. The models include non-equilibrium primordial gas chemistry and cooling processes and accurate radiation transport in the Case B approximation using adaptively ray traced photon packages, retaining the time derivative in the transport equation. Supernova feedback is modeled by thermal explosions triggered at parsec scales. All calculations resolve the local Jeans length by at least 16 grid cells at all times and as such cover a spatial dynamic range of $\sim$$10^6$. These first sources of reionization are highly intermittent and anisotropic and first photoionize the small scales voids surrounding the halos they form in, rather than the dense filaments they are embedded in. As the merging objects form larger, dwarf sized galaxies, the escape fraction of UV radiation decreases and the H II regions only break out on some sides of the galaxies making them even more anisotropic. In three cases, SN blast waves induce star formation in overdense regions that were formed earlier from ionization front instabilities. These stars form tens of parsecs away from the center of their parent DM halo. Approximately 5 ionizing photons are needed per sustained ionization when star formation in 10^6 $M_\odot$ halos are dominant in the calculation. As the halos become larger than $\sim$$10^7 M_\odot$, the ionizing photon escape fraction decreases, which in turn increases the number of photons per ionization to 15–50, in calculations with stellar feedback only. Supernova feedback in these more massive halos creates a more diffuse medium, allowing the stellar radiation to escape more easily and maintaining the ratio of 5 ionizing photons per sustained ionization.

Subject headings: cosmology: theory — intergalactic medium — galaxies: formation — stars: formation

1. MOTIVATION

It is clear that quasars are not responsible to keep the universe ionized at redshift 6. The very brightest galaxies at those redshifts alone also provide few photons. The dominant sources of reionization so far are observationally unknown despite remarkable advances in finding sources at high redshift (e.g. Shapiro 1986; Bouwens et al. 2004; Fan et al. 2006; Thompson et al. 2007; Eyles et al. 2006) and hints for a large number of unresolved sources at very high redshifts (Spergel et al. 2007; Kashlinsky et al. 2007) which is still a topic of debate (Cooray et al. 2007; Thompson et al. 2007). At the same time, ab initio numerical simulations of structure formation in the concordance model of structure formation have found that the first luminous objects in the universe are formed inside of cold dark matter (CDM) dominated halos of total masses $2 \times 10^5 - 10^6 M_\odot$ (Haiman et al. 1996; Tegmark et al. 1997; Abel et al. 1998). Fully cosmological ab initio calculations of Abel et al. (2000, 2002) and more recently Yoshida et al. (2006) clearly show that these objects will form isolated very massive stars. Such stars will be copious emitters of ultraviolet (UV) radiation and are as such prime suspect to get the process of cosmological reionization started. In fact, one dimensional calculations of Whalen et al. (2004) and Kitayama et al. (2004) have already argued that the earliest H II regions will evaporate the gas from the host halos and that in fact most of the UV radiation of such stars would escape into the intergalactic medium. Recently, Yoshida et al. (2007a) and Abel et al. (2007) demonstrated with full three-dimensional radiation hydrodynamical simulations that indeed the first H II regions break out of their host halos quickly and fully disrupt the gaseous component of the cosmological parent halo. All of this gas finds itself radially moving away from the star at $\sim$ 30 km s^{-1} at a distance of $\sim$ 100 pc at the end of the stars life. At this time, the photo-ionized regions have now high electron fractions and little destructive Lyman-Werner band radiation fields creating ideal conditions for molecular hydrogen formation which may in fact stimulate further star formation above levels that would have occurred without the pre-ionization. Such conclusion have been obtained in calculations with approximations to multi dimensional radiative transfer or one dimensional numerical models (Ricotti et al. 2002a; Nagakura & Omukai 2005; O'Shea et al. 2005; Yoshida et al. 2006; Ahn & Shapiro 2007; Johnson et al. 2007). These early stars may also explode in supernovae and rapidly enrich the surrounding material with heavy elements, deposit kinetic energy and entropy to the gas out of which subsequent structure is to form. This illustrates some of the complex interplay of star formation, primordial gas chemistry, radiative and supernova feedback and readily explains why any reliable results will only be obtained using full ab initio three dimensional hydrodynamical simulations. In this paper, we present the most detailed such calculations yet carried out to date and discuss issues important to the un-

---

Electronic address: john.h.wise@nasa.gov
[1] Kavli Institute for Particle Astrophysics and Cosmology, Stanford University, Menlo Park, CA 94025
[2] Current address: Laboratory for Observational Cosmology, NASA Goddard Space Flight Center, Greenbelt, MD 21114

Submitted to Astrophysical Journal

Work supported in part by US Department of Energy contract DE-AC02-76SF00515

TABLE 1
Simulation Parameters

Name	l [Mpc]	Cooling model	SF	SNe	$N_{\rm part}$	$N_{\rm grid}$	$N_{\rm cell}$
SimA-Adb	1.0	Adiabatic	No	No	2.22×10^7	30230	9.31×10^7 (453^3)
SimA-HHe	1.0	H, He	No	No	2.22×10^7	40601	1.20×10^8 (494^3)
SimA-RT	1.0	H, He, H_2	Yes	No	2.22×10^7	44664	1.19×10^8 (493^3)
SimB-Adb	1.5	Adiabatic	No	No	1.26×10^7	23227	6.47×10^7 (402^3)
SimB-HHe	1.5	H, He	No	No	1.26×10^7	21409	6.51×10^7 (402^3)
SimB-RT	1.5	H, He, H_2	Yes	No	1.26×10^7	24013	6.54×10^7 (403^3)
SimB-SN	1.5	H, He, H_2	Yes	Yes	1.26×10^7	24996	6.39×10^7 (400^3)

Note. — Col. (1): Simulation name. Col. (2): Box size. Col. (3): Cooling model. Col. (4): Star formation. Col. (5): Supernova feedback. Col. (6): Number of dark matter particles. Col. (7): Number of AMR grids. Col. (8): Number of unique grid cells.

derstanding of the process of cosmological reionization.

It is timely to develop direct numerical models of early structure formation and cosmological reionization as considerable efforts are underway to

1. Observationally find the earliest galaxies with the James Webb Space Telescope (JWST; Gardner et al. 2006) and the Atacama Large Millimeter Array (ALMA; Wilson et al. 2005),
2. Further constrain the amount and spatial non-uniformity of the polarization of the cosmic microwave background radiation (Page et al. 2007),
3. Measure the surface of reionization with LOFAR (Rottgering et al. 2006), MWA (Bowman et al. 2007), GMRT (Swarup et al. 1991) and the Square Kilometer Array (SKA; Schilizzi 2004), and
4. Find high redshift gamma ray bursts with SWIFT (Gehrels et al. 2004) and their infrared follow up observations.

We begin by describing the cosmological simulations that include primordial star formation and accurate radiative transfer. In §3, we report the details of the star formation environments and host halos in our calculations. Then in §4, we describe the resulting start of cosmological reionization, and investigate the environments in which these primordial stars form and the evolution of the clumping factor. We compare our results to previous calculations and further describe the nature of the primordial star formation and feedback in §5. Finally we summarize our results in the last section.

2. RADIATION HYDRODYNAMICAL SIMULATIONS

We use radiation hydrodynamical simulations with a modified version of the cosmological AMR code *Enzo* to study the radiative effects from the first stars (Bryan & Norman 1997, 1999). We have integrated adaptive ray tracing (Abel & Wandelt 2002) into the chemistry, energy, and hydrodynamics solvers in *Enzo* that accurately follow the evolution of the H II regions from stellar sources and their relevance during structure formation and cosmic reionization.

Seven different simulations are discussed here. Table 1 gives an overview of the parameters and the physics included in these calculations. We perform two cosmological realizations, Sim A and B, with three sets of assumptions about the primordial gas chemistry. The simplest calculations here assume only adiabatic gas physics and provide the benchmark against which the more involved calculations are compared. We compare this to one model with atomic hydrogen and helium cooling only and one that includes H_2 cooling. Massive, metal-free star formation is included only in the H_2 cooling models.

These calculations are initialized at redshift[3] $z = 130$ (120) when the intergalactic medium has a temperature of 325 (280) K in box sizes 1 comoving Mpc (1.5 Mpc) for Sim A (B). We use the cosmological parameters of $(\Omega_B h^2,\ \Omega_M,\ h,\ \sigma_8,\ n) = (0.024,\ 0.27,\ 0.72,\ 0.9,\ 1)$ from first year WMAP results, where the constants have the usual meaning (Spergel et al. 2003). The changes in the third year WMAP results (Spergel et al. 2007) does not affect the evolution of individual halos studied here but only delays structure formation by ∼40% (Alvarez et al. 2006b). The adiabatic simulations as well as the atomic hydrogen and helium cooling only calculations are described in Wise & Abel (2007a). The new models presented here have the exact same setup and random phases in the initial density perturbation and only differ in that they include star formation as well as follow the full radiation hydrodynamical evolution of the H II regions and supernova feedback in Sim B. We use the designations RT and SN to distinguish cases in which only star formation and radiation transport were included (RT) and the one model which also includes supernovae (SN) in Sim B. We use the same refinement criteria as in our previous work, where we refine if the DM (gas) density becomes three times greater than the mean DM (gas) density times a factor of 2^l, where l is the AMR refinement level. We also refine to resolve the local Jeans length by at least 16 cells. Cells are refined to a maximum AMR level of 12 that translates to a spatial resolution of 1.9 (2.9) comoving parsecs. This spatial resolution of ∼0.1 proper pc is required to model the formation of the D-type front at small scales correctly. Refinement is restricted to the innermost initial nested grid that has a side length of 250 (300) comoving kpc.

The star formation recipe and radiation transport are detailed in Wise & Abel (2007c). Here we overview the basics about our method. Star formation is modelled using the Cen & Ostriker (1992) algorithm with the additional requirement that an H_2 fraction of 5×10^{-4} must

---

[3] To simplify the discussion, simulation A will always be quoted first with the value from simulation B in parentheses.

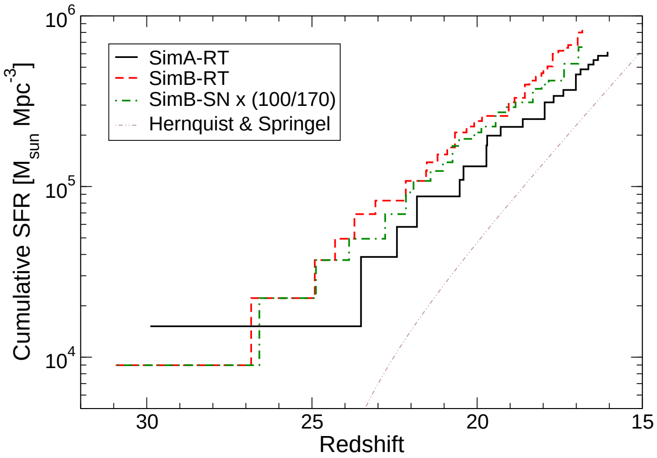

FIG. 1.— Cumulative star formation rate in units of comoving $M_\odot$ Mpc^{-3} of SimA-RT (solid), SimB-RT (dashed), and SimB-SN (dot-dashed). The star formation rate of SimB-SN has been scaled by 100/170, which is the ratio of Pop III stellar masses used in SimB-RT and SimB-SN, in order to make a direct comparison between the two simulations. The dot-dot-dashed line represents the cumulative star formation rate in atomic hydrogen cooling halos from Hernquist & Springel (2003).

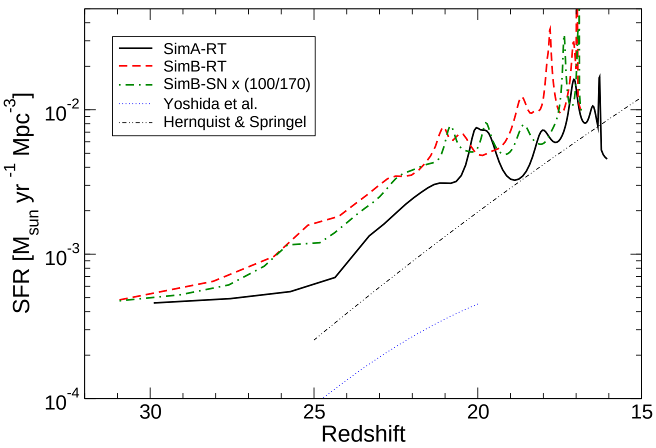

FIG. 2.— Comoving star formation rate in units of M$_\odot$ yr^{-1} Mpc^{-3}. The lines representing the simulation data have the same meaning as in Figure 1. The crosses show at which redshifts stars form. The rates in SimB-SN are scaled for the same reason as in Figure 1. For comparison, we overplot the star formation rates from Hernquist & Springel (2003) in atomic hydrogen line cooling halos and Yoshida et al. (2003) for $100 M_\odot$ Pop III stars.

exist before a star forms. We allow star formation to occur in the Lagrangian volume of the surrounding region out to three virial radii from the most massive halo at $z = 10$ in the dark matter only runs as discussed in Wise & Abel (2007a). This volume that has a side length of 195 (225) comoving kpc at $z = 30$ and 145 (160) comoving kpc at the end of the calculation. The calculations with SNe use a stellar mass $M_\star$ of $170 M_\odot$, whereas the ones without SNe use a mass of $100 M_\odot$. The ionizing luminosities are taken from no mass loss models of Schaerer (2002), and we employ the SN energies from Heger & Woosley (2002). Star particles after main sequence are tracked but are inert. There is evidence of lower mass primordial stars forming within relic H II regions (O'Shea et al. 2005; Yoshida et al. 2007b), but we neglect this to avoid additional uncertain parameters. This is a desired future improvement, however.

We use adaptive ray tracing (Abel & Wandelt 2002) to calculate the photo-ionization and heating rates caused by stellar radiation. We consider photo-ionization from photons with an energy of 28.4 (29.2) eV that is the mean energy of ionizing radiation from a metal-free star with 100 (170) $M_\odot$. We account for H_2 photo-dissociation with a $1/r^2$ Lyman-Werner radiation field without self-shielding. We use a non-equilibrium, nine-species (H, H^+, He, He^+, He^{++}, e^-, H_2, H_2^+, H^-) chemistry solver in *Enzo* (Abel et al. 1997; Anninos et al. 1997) that takes into account the additional spatial dependence of the photoionization rates provided by the radiation transport.

We end the simulations when the most massive halo begins to rapidly collapse (i.e. $t_{\rm cool} < t_{\rm dyn}$) in the hydrogen and helium cooling only runs at redshift 15.9 (16.8). The virial temperature $T_{\rm vir}$ of the halo is $\sim 10^4$ K at these redshifts.

3. STAR FORMATION

Here we describe the aspects of massive metal-free star formation in our simulations. The first star forms at redshift 29.7 (30.8) in halo typical of Pop III star formation without any feedback that has a mass of $\sim 5 \times 10^5 M_\odot$ (cf. Abel et al. 2000, 2002; Machacek et al. 2001; Yoshida et al. 2003, 2006). Afterwards there are a total of 19, 29, and 24 instances of star formation in SimA-RT, SimB-RT, and SimB-SN, respectively.

3.1. *Star Formation Rate*

We show the cumulative star formation rate (SFR) in units of comoving $M_\odot$ Mpc^{-3} in Figure 1. This quantity is simply calculated by taking the total mass of stars formed at a given redshift divided by the comoving volume where stars are allowed to form (see §2). In this figure, we decrease the SFR of SimB-SN by a factor of 1.7 in order to directly compare the rates from the other two simulations. This minimizes some of the uncertainties entered into our calculations when we chose the free parameter of Pop III stellar mass. The cumulative rates are very similar in both realizations. The refined volume of Sim A (Sim B) has an average overdensity $\delta \equiv \rho/\bar{\rho} =$ 1.4 (1.8). The more biased regions in Sim B allows for a higher density of star-forming halos that leads to the increased cumulative SFR.

We also overplot the cumulative SFR in atomic hydrogen cooling halos from Hernquist & Springel (2003) in this figure. It is up to an order of magnitude lower than the rates seen in our calculations up to redshift 20. They only focused on larger mass halos in their simulations. The disparity between the rates is caused by our simulations only sampling a highly biased region, where we focus on a region containing a 3-σ density fluctuation, and from the contribution from Pop III stars. The rates of Hernquist & Springel (2003) are calculated from an extensive suite of smoothed particle hydrodynamics simulations that encompasses both large and small simulation volumes and give a more representative global SFR due to their larger sampled volumes. However, our adaptive spatial resolution allows us to study both the small- and large-scale radiative feedback from Pop III stars, which is the main focus of the paper, in addition

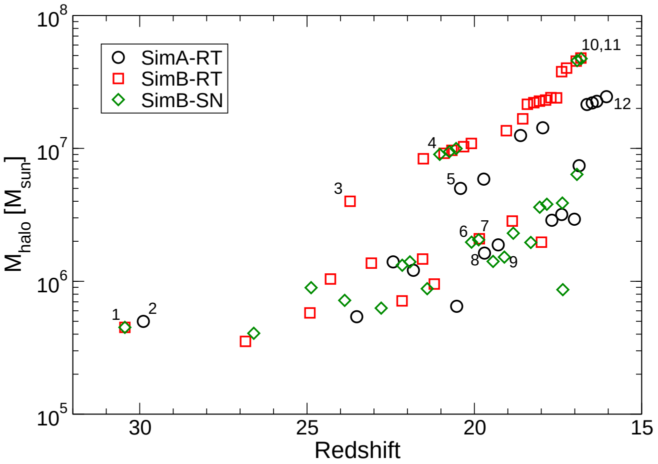

FIG. 3.— Star formation times versus host halo DM mass for SimA-RT (circles), SimB-RT (squares), and SimB-SN (triangles). One symbol represents one star. The numbers correspond to the halo numbers listed in Table 2.

TABLE 2
SELECTED STAR FORMING HALO PARAMETERS

#	Sim	Type	z	M_{vir} [$M_\odot$]	f_b	ρ_c [cm^{-3}]	T_c [K]
1	SimB-RT	1	30.9	4.7×10^5	0.081	1600	340
2	SimA-RT	1	29.9	4.8×10^5	0.094	6500	350
3	SimB-RT	4	23.7	5.3×10^6	0.059	2400	410
4	SimB-SN	4	21.0	1.1×10^7	0.045	1800	480
5	SimA-RT	4	20.4	6.3×10^6	0.069	550	440
6	SimB-SN	2	20.1	2.6×10^6	0.12	120	390
7	SimB-RT	2	19.9	2.8×10^6	0.12	870	450
8	SimA-RT	2	19.3	2.9×10^6	0.13	1300	440
9	SimB-SN	3	19.3	2.3×10^6	0.12	360	450
10	SimB-RT	5	16.8	3.1×10^7	0.089	4100	2500
11	SimB-SN	5	16.8	2.9×10^7	0.065	1100	590
12	SimA-RT	5	16.1	3.0×10^7	0.061	130	470

NOTE. — Col. (1): Halo number. Col. (2): Simulation source. Col. (3): Star formation type. Col. (4): Redshift. Col. (5): Virial mass. Col. (6): Baryon mass fraction. Col. (7): Central number density. Col. (8): Central temperature.

to the quantitative measures such as a SFR.

To estimate a SFR (i.e. Madau et al. 1996, in units of comoving $M_\odot$ yr^{-1} Mpc^{-3}) from the cumulative SFR, we first fit the cumulative SFR with a cubic spline with 10 times the temporal resolution. Then we smooth the data back to its original time resolution and evaluate its time derivative to obtain the SFR that we show in Figure 2. We also mark the redshifts of star formation with crosses. We again compare our rates to ones calculated in Hernquist & Springel (2003) for metal-enriched stars and Yoshida et al. (2003) for Pop III stars with a mass of 100 $M_\odot$. Our rates are higher for reasons discussed previously. We do not advocate these SFRs as cosmic averages but give them as a useful diagnostic of the performed simulations.

We see an increasing function from 5×10^{-4} $M_\odot$ yr^{-1} Mpc^{-3} at redshift 30 to $\sim 6 \times 10^{-3}$ $M_\odot$ yr^{-1} Mpc^{-3} at redshift 20. Here only one star per halo forms in objects with masses $\lesssim 5 \times 10^6 M_\odot$. Above this mass scale, star formation is no longer isolated in nature and can be seen by the bursting nature of the star formation after redshift 20, where the SFR fluctuates around 10^{-2} $M_\odot$ yr^{-1} Mpc^{-3} (cf. Ricotti et al. 2002b). Since we neglect H_2 self-shielding, the strong Lyman-Werner (LW) radiation dissociates almost all H_2 in the host halo and surrounding regions. Thus we rarely see simultaneous instances of star formation. However, the regions that were beginning to collapse when a nearby star ignites form a star 3 – 10 million years after the nearby star dies. This only results in a minor change in the timing of star formation. Furthermore this delay is minimal compared to the Hubble time and does not affect SFRs.

3.2. *Star Forming Halo Masses*

We show the star formation times versus the host halo DM masses as a function of redshift in Figure 3. The DM halo masses are calculated with the HOP algorithm (Eisenstein & Hut 1998). First we focus on star formation in the largest halo. Around redshift 30, the first star forms in all three simulations with a mass of $\sim 5 \times 10^5 M_\odot$. The stellar radiation drives a $\sim$30 km s^{-1} shock wave that removes almost all of the gas from the shallow potential well. It takes approximately 75 (40) million years for gas to reincorporate into the potential well from smooth IGM accretion and mergers. At $z \sim 24$ in SimB-RT, the second star forms in the most massive progenitor that now has a mass of $4 \times 10^6 M_\odot$. In SimA-RT, the merger history is calmer at $z = 24 - 30$, and enough gas becomes available for H_2 cooling and star formation at $z \sim 20$. Here the second star forms in the most massive progenitor that has a mass of $5 \times 10^6 M_\odot$. In both RT simulations, the stellar feedback expels most of the gas from its host once again. For Sim A (Sim B), another 10 (30) million years passes before the next star to form in this halo. Once the halo has a mass of $\sim 10^7$ $M_\odot$, the potential energy is great enough to confine most of the stellar and SNe outflows. In SimA-RT and SimB-RT, halos above this mass scale host multiple sites of star formation that is seen in the nearly continuous bursts of star formation in the most massive halo. SimA-RT forms stars more intermittently than SimB-RT because it undergoes two major mergers between redshift 17 and 21 (see Wise & Abel 2007a). In SimB-SN at $z = 21$, three stars form in succession in the most massive halo. Their aggregate stellar and SNe feedback expels the gas from its halo one more time. This halo only forms another star at $z = 16.9$ (55 million years later) in this halo when enough gas has been reincorporated.[4]

Most of the stars form in low-mass halos with masses $\sim 10^6$ $M_\odot$ that are forming its first star between redshifts 18 – 25 in our calculations. A slight increase in host halo masses with respect to redshift mainly occurs because of the negative feedback from photo-evaporation of low-mass halos that are close to other star-forming halos (Haiman et al. 2001). Additional delays in star formation may be caused by ultraviolet heating and H_2 dissociation from previous stars (e.g. Machacek et al. 2001; Yoshida et al. 2003; Mesigner et al. 2006), which increase the critical halo mass in which gas can cool and condense.

One interesting difference in SimB-SN from the other calculations is that star formation is sometimes induced in overdensities within the same halo when a SN blast

---

[4] We have run SimB-SN past $z = 16.8$ and have seen that it starts to host multiple sites of star formation.

wave overtakes it. This occurs in three halos with masses of 2.0, 1.5, and 3.8 $\times 10^6 M_\odot$ at redshifts 19.9, 19.1, and 17.8, respectively. The same halos in SimB-RT do not form two stars before their gas are expelled and thus quenching subsequent star formation.

3.3. *Star Formation Environments*

We further study the nature of high-redshift star formation by selecting four star forming regions from each simulation and studying the surrounding interstellar medium (ISM) prior to star formation. The ISM in the 10^4 K halos are described in more detail in Wise & Abel (2007c). The sample of regions are chosen in order to compare different star formation environments. These regions can be categorized into (1) first star inside an undisturbed halo, (2) first star that is delayed by LW radiation, (3) induced star formation by positive feedback, (4) star formation after gas reincorporation, and (5) star formation in a halo with a virial temperature over 10^4 K. The represented halos and their parameters are listed in Table 2 and annotated in Figure 3.

We plot the mass-weighted radial profiles of number density (left columns) and temperature (right columns) within the virial radius for these twelve halos in Figure 4 and describe them below.

1. *First star* (Halo 1, 2)— These stars are the first to form in their respective simulation volume. The structure of the host halos within our resolution limit exhibit similar characteristics, e.g., a self-similar collapse and central temperatures of 300 K, as in previous studies (Abel et al. 2000, 2002; Bromm et al. 2002; Yoshida et al. 2006). The halo masses are $4.8(4.7) \times 10^5$ $M_\odot$. Heating from virialization raises gas temperatures to 3000 K, and in the central parsec, H_2 cooling becomes effective and cools the gas down to 200 K that drives the further collapse. The mass-weighted central gas densities and temperatures are approximately 3000 cm^{-3} and 320 K, respectively.

2. *Delayed first star* (Halo 6, 7, 8)— The host halos have similar radial profiles as the halos that hosted the first stars but with masses of $\gtrsim 10^6 M_\odot$. Here the H_2 cooling has been stifled by the LW radiation from nearby star formation. Only when the halo mass passes a critical mass, the core can cool and condense by H_2 formation (Machacek et al. 2001; Yoshida et al. 2003; O'Shea & Norman 2007; Wise & Abel 2007b). The central densities are lower than the first stars with 1300, 870, and 120 cm^{-3} in SimA-RT, SimB-RT, and SimB-SN, respectively. The central temperatures are marginally higher at 440, 450, and 390 K.

3. *Induced star formation* (Halo 9)— At $z = 19.3$, a massive star explodes in a SN, whose shell initially propagates outward at 4000 km s^{-1}. After 160 kyr, the shell passes an overdensity within the same halo that is caused by an ionization front instability (e.g., see Whalen & Norman 2007a,b). The star forms 35 pc away from the SN explosion and the DM halo center. The combination of the shock passage and excess free electrons in the relic H II catalyze H_2 formation in this low-mass halo (e.g. Ferrara 1998; O'Shea et al. 2005; Mesigner et al. 2006). The SN blast wave heats the gas over 10^4 K to radii as 1 pc. In the density profile, both low and high density gas exists at similar radii. Here the shock passage creates a tail of gas streaming from the central core, whose asymmetries can be seen in the density profile. However, the core survives and benefits from the excess electrons created during this event. The central temperature is similar to the previous cases at 450 K. The H_2 criterion for star formation is reached faster because of the excess electrons, which creates a star particle at a lower density (360 cm^{-3}).

4. *Star formation after reincorporation* (Halo 3, 4, 5)— After a sufficient amount of gas that was expelled by dynamical feedback of the first star is reincorporated into the halo, star formation is initiated again. Here virial temperatures of the halos are under 10^4 K, which are hosting their second instance of star formation. These halos have a larger spread in gas densities and temperatures than the halos forming their first star. Gas is heated by virialization and prior stellar radiation to over 10^4 K outside 10 pc. The central densities in halos 3 and 5 are similar to the regions described in the first star formation section, however they are slightly warmer at 410 and 480 K. Halo 4 shows a more diffuse core with densities of 550 cm^{-3} and temperatures of 440 K.

5. *Star formation in 10^4K halos* (Halo 10, 11, 12)— In these halos, H_2 formation is aided by atomic hydrogen cooling. The ISM becomes increasingly complex as more stars form in the halo. The temperatures range from 100 K to 20,000 K throughout the halo. Halos 10 and 12 have hosted 16 and 8 massive stars, respectively, since it started to continually form stars at $z \sim 20$. In SimB-RT (halo 10), the densities are higher than the cases. The gas in this halo is more centrally concentrated than the others because the H II regions did not breakout of the halo, thus minimizing any outflows from feedback and dispersion of the central core. The temperature in halo 10 is significantly warmer than other regions at 2500 K. In halo 11, the devastation caused by three stars and their SNe at $z = 21$ prevented star formation until $z = 16.9$. Its initial recovery from that event is apparent by the single cool core with a temperature of 590 K that sharply transitions to a warm, diffuse medium at $r = 10$ pc. Halo 12 (SimA-RT) has a complex morphology that is not centrally concentrated and is caused by stellar outflows during a major merger (see Wise & Abel 2007c, for images). This morphology manifests itself in the radial profiles as large density contrasts spanning nearly six order of magnitude at $r = 30 - 300$ pc. Similarly, temperatures range from 50 K to 10,000 K in the same region. The star forms in a diffuse region ($\rho = 130$ cm^{-3}) that has a temperature of 470 K and whose H_2 formation is enhanced because it resides in a relic H II region.

4. STARTING COSMOLOGICAL REIONIZATION

In this section, we first describe the ionizing radiation from massive stars that start cosmological reionization in small overdense regions we simulate. Then we discuss the effects of recombinations in the inhomogeneous IGM and kinetic energy feedback from Pop III stars. Lastly the evolution of the average IGM thermal energy is examined.

To illustratively demonstrate radiative feedback from massive stars on the host halos and IGM, we show pro-

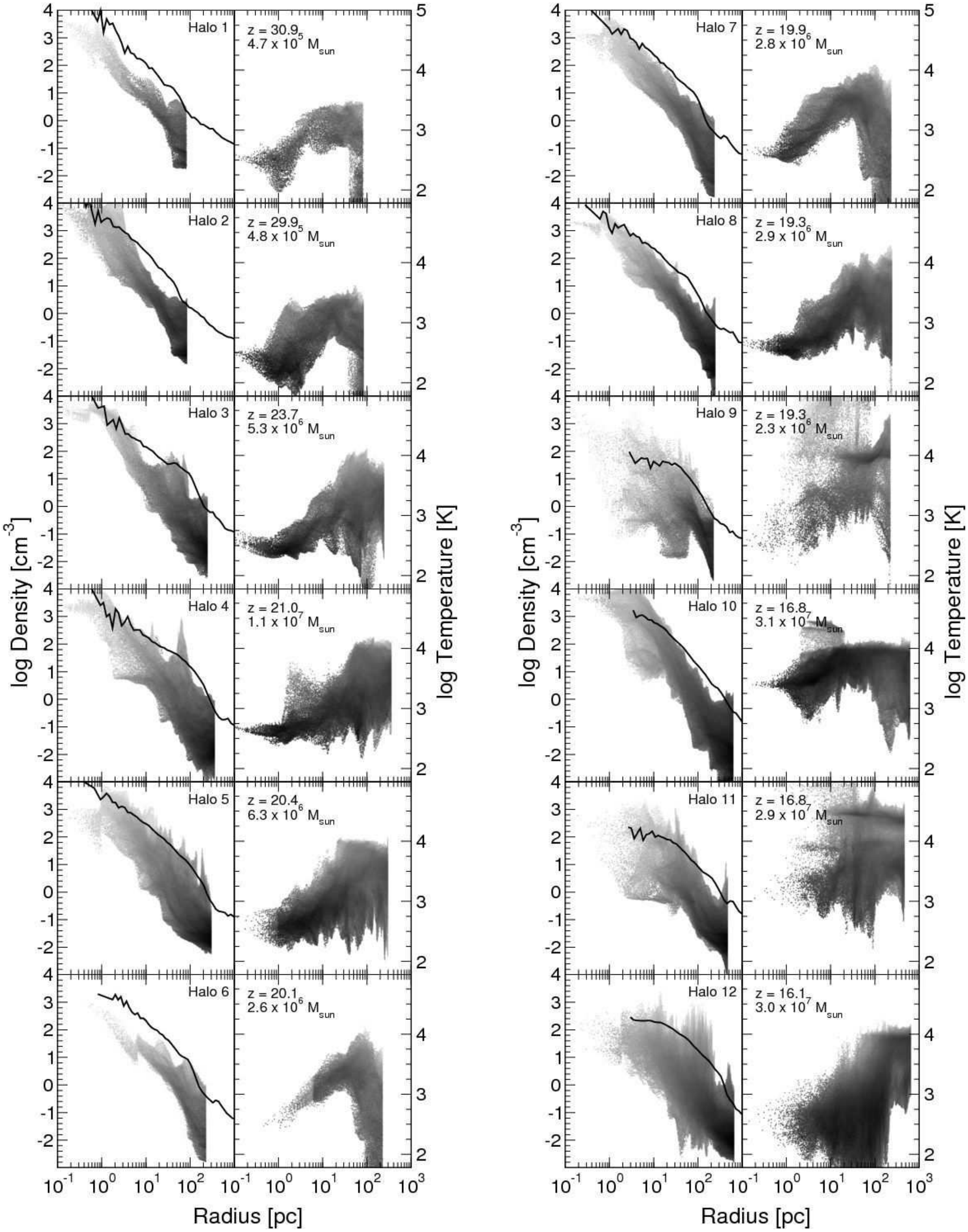

FIG. 4.— Radial profiles of number density (left column) and temperature (right column) for selected star forming halos inside the virial radius. We overplot the radially averaged DM density (solid line) in units of m_h cm^{-3}. These data represent the state of the region immediately after star formation. Notice the added complexity (range) in the density and temperature with increasing host halo mass, especially if the region has been affected by stellar radiation, as in Halos 3, 4, 5, 10, 11, and 12. The occasional discontinuities in density in the inner parsec arise from our star formation recipe when we remove half the mass in a sphere containing twice the stellar mass.

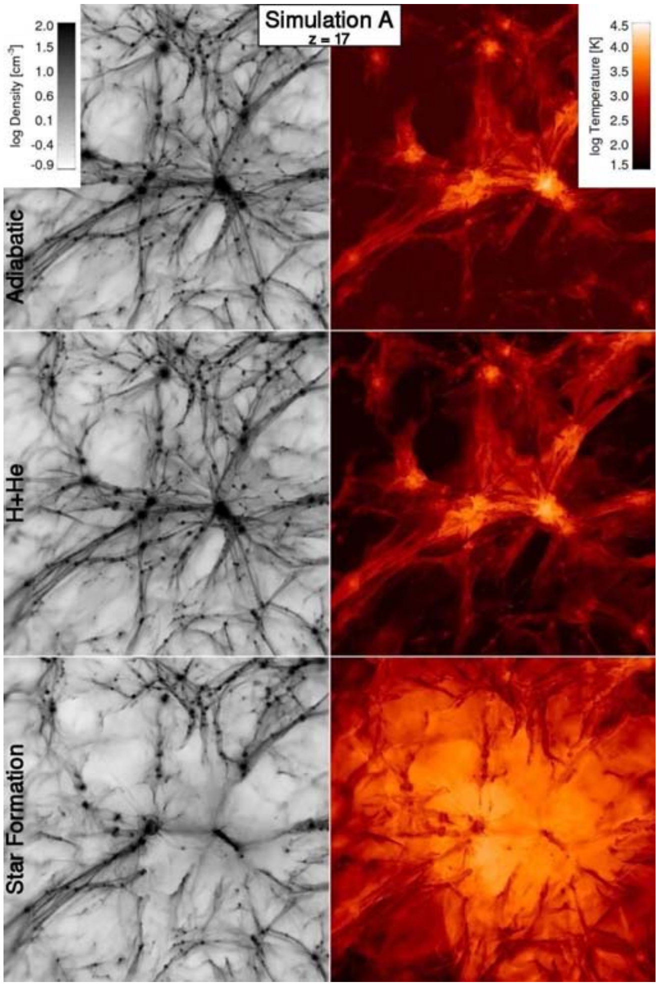

FIG. 5.— Density-squared weighted projections of gas density (left) and temperature (right) of Sim A. The field of view is 8.5 proper kpc (1/216 of the simulation volume) and the color scale is the same for all simulations.

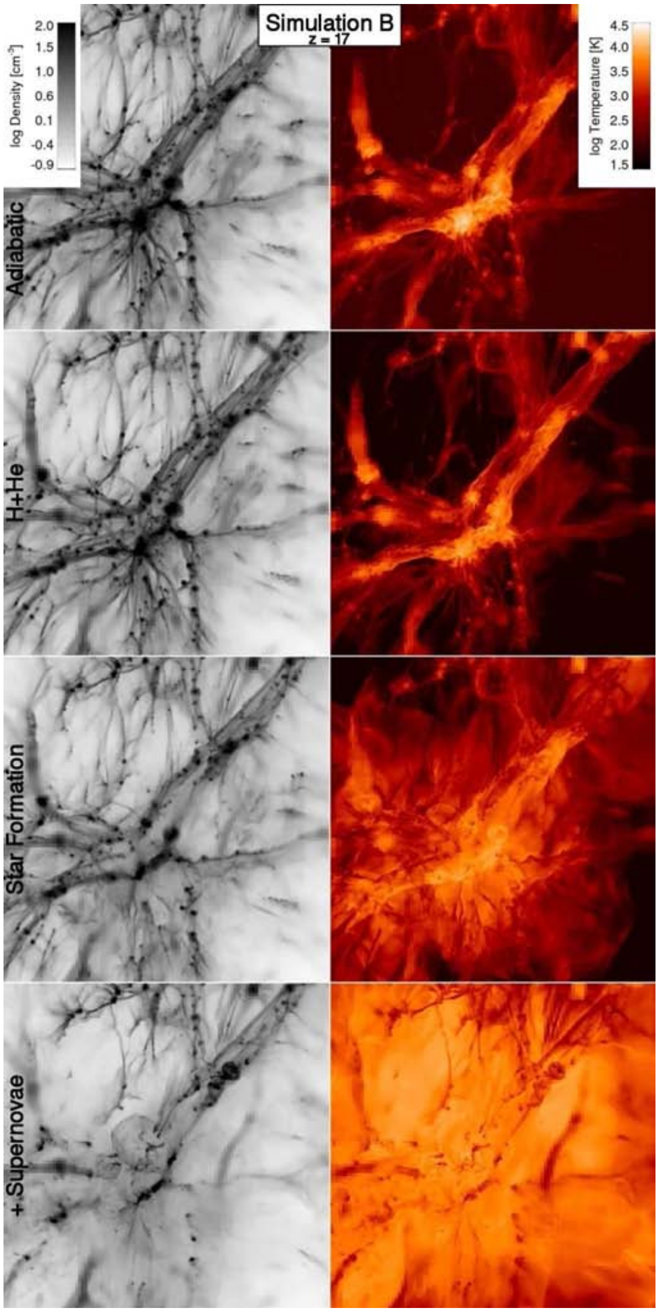

FIG. 6.— Same as Figure 5 but for Sim B.

jections of gas density and temperature that are density-squared weighted in Figures 5 and 6 for all of the simulations at redshift 17. These projections have the same field of view of 8.5 proper kpc and the same color maps. The large-scale density structure is largely unchanged by the stellar feedback, and the adjacent filaments remain cool since they are optically thick to the incident radiation. H_2 cooling produces more centrally concentrated objects; however stellar feedback photo-evaporates $\lesssim 10^6 M_\odot$ halos near other star-forming halos. This is apparent in the density projections in the Jeans smoothing around the most massive halo (cf. Haiman et al. 2001; Mesigner et al. 2006). Kinematic feedback from SNe has an even larger effect on the surrounding gas. In SimB-SN, this effect is seen in the reduced small-scale structure and low-mass halos with no gas counterparts. However, the most apparent difference in the radiative simulations is the IGM heating by Pop III stars, especially in SimB-SN.

4.1. *UV Emissivity*

A key quantity in reionization models is volume-averaged emissivity of ionizing radiation. We utilize the comoving SFR $\dot{\rho}_\star$ to calculate the proper volume-averaged UV emissivity

$$\epsilon = \frac{\dot{\rho}_\star Q_{\rm HI} t_{\rm H}}{\bar{\rho}_b} \tag{1}$$

in units of ionizing photons per baryon per Hubble time. Here $Q_{\rm HI}$ is the number of ionizing photons emitted in the lifetime of a star per solar mass, $\bar{\rho}_b \simeq 2 \times 10^{-7}$ is the comoving mean number density, and

$$t_{\rm H} \approx \frac{2}{3H_0\sqrt{\Omega_m}}(1+z)^{-3/2} \tag{2}$$

is the Hubble time in a Einstein de-Sitter universe, which is valid for ΛCDM cosmology at $z \gg 1$. For a Pop III stellar masses greater than 100 $M_\odot$, $Q_{\rm HI} \approx 10^{62}$ photons

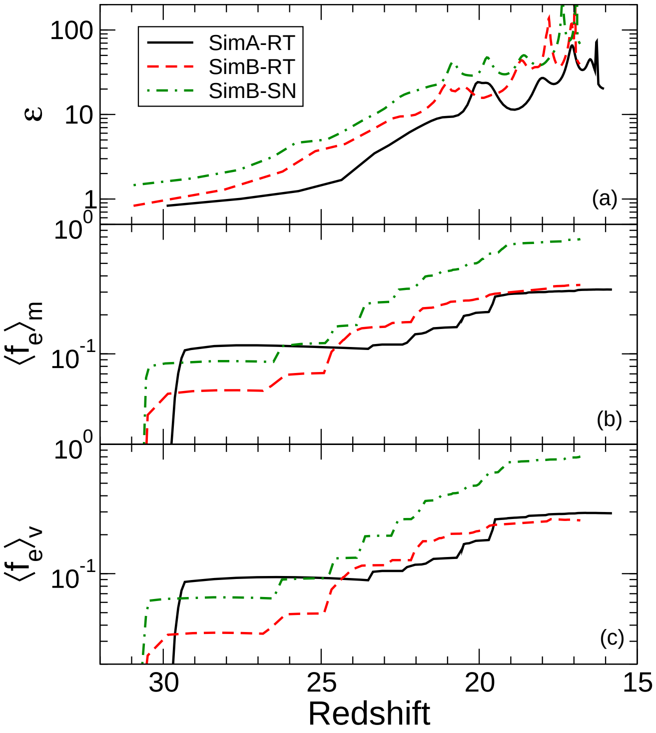

FIG. 7.— (a) Averaged emissivity in units of ionizing photons per baryon per Hubble time that is calculated from the star formation rate in Figure 2. (b) Mass-averaged ionization fraction of the inner 250 (300) comoving kpc for SimA (SimB). (c) Volume-averaged ionization fraction for the same runs.

per solar mass, corresponding to 84000 ionizing photons per stellar proton (Schaerer 2002). We plot the emissivity ϵ in Figure 7a. It follows the same behavior as the SFR, but now can be directly used in semi-analytic reionization models. The emissivity increases from unity at redshift 30 to ∼100 at the end of our simulations. Our results agree with the emissivity calculated in semi-analytic models that include Pop III stars (e.g. Onken & Miralda-Escudé 2004) and should be an upper limit however.

4.2. *Effective Number of Ionizations per UV Photon*

We show the mass-averaged and volume-averaged ionization fraction f_e within the refined region in Figures 7b and 7c. The first star in the simulation ionizes between 5–10% of the volume where we allow star formation. As stars begin to form in other halos after redshift 25, the ionization fraction gradually builds to 30% in the RT simulations and 75% in the SN case. The higher stellar luminosities in SimB-SN, which can be seen in Figure 7a, and the additional outflows generated by SN blast waves cause this difference in f_e. Additionally, the H II regions in halos with sustained star formation in the RT simulations do not fully breakout into the IGM. Kitayama et al. (2004) provided a useful approximation of the critical halo mass

$$M_{\rm crit}^{\rm ion} \sim 2.5 \times 10^6 \left(\frac{M_\star}{200 M_\odot}\right)^{3/4} \left(\frac{1+z}{20}\right)^{-3/2} M_\odot, \quad (3)$$

in which an ionization front (I-front) cannot escape. This approximation is valid for stellar masses between 80 and 500 $M_\odot$, redshifts between 10 and 30, and singular isothermal spheres. Our simulations exhibit this same trait in which I-fronts only partially breakout from the host halo above this mass scale.

This is not the case with SNe because previous SN blast waves can more effectively evacuate the surrounding medium, thus increasing the chances of radiation escaping into the IGM from later stars in the same halo. At $z = 21$, there is an example of this occurring with three stars forming in succession in the most massive halo. After the first star goes SN, a diffuse and hot medium is left behind, but the blastwave has not completely disrupted two other nearby condensing clumps. The radiation from the second star now does not have to ionize its host halo and has an escape fraction of near unity. The same happens for the third star in this halo. This episode further ionizing SimB-SN from 40% to 60%. As a note of caution, these ionized fractions should not be considered as cosmological average because they only sample a highly biased region. Iliev et al. (2006) showed that a simulation box size of ∼30 Mpc is needed to make global predictions.

To examine the strength of recombinations, we compare the total number of electrons in the volume to the total number of ionizing photons emitted in Figure 8. The ratio of these two quantities is the number of UV photons needed for one effective ionization initially. This ratio is approximately 3/5 (1/3) after the first star dies. The values in simulation A are higher due to its smaller volume. This ratio then steadily decreases from recombinations in the relic H II region to a few percent when the next star forms. As stars begin to form regularly in the simulation, there are 4 (6) photons per sustained ionization. However this ratio drops by a factor of 5 in the RT simulations after $z \sim 20$ when the H II regions become trapped in the halo, thus reducing the available photons for ionizing the IGM. The effects of SNe as previously discussed maintains the ratio of 6 photons required per ionization as the most massive halo grows in mass.

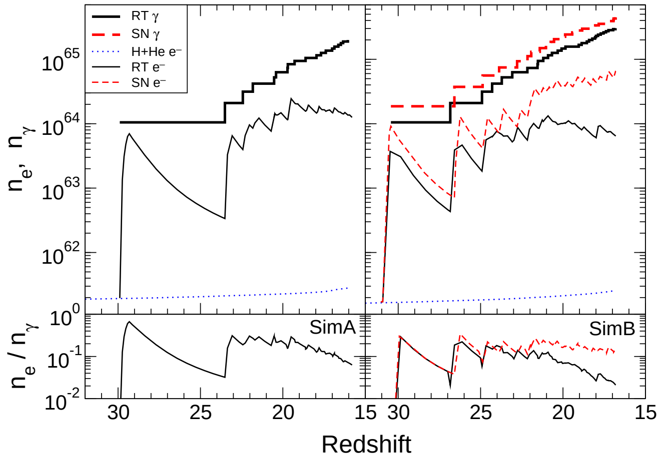

FIG. 8.— *Top panels*: Total number of ionizing photons emitted (thick lines) and total number of electrons (thin lines) for simulations with cooling only (dotted), star formation only (solid), and supernovae (dashed) in the inner 250 and 300 comoving kpc for SimA (left) and SimB (right). The H II regions are completely contained in these volumes. *Bottom panels*: The ratio of total number of electrons to the total number of ionized photons emitted.

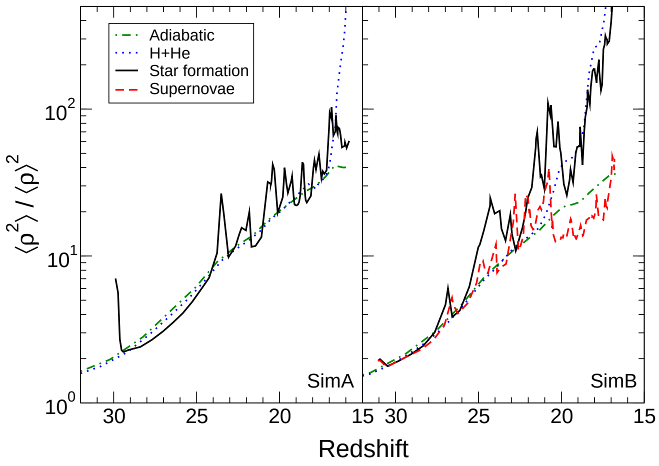

FIG. 9.— Clumping factor $C = \langle\rho^2\rangle/\langle\rho\rangle^2$ for SimA (left) and SimB (right), comparing the cases of the adiabatic equation of state (dot-dashed), atomic hydrogen and helium cooling (dotted), star formation only (solid), and supernovae (dashed).

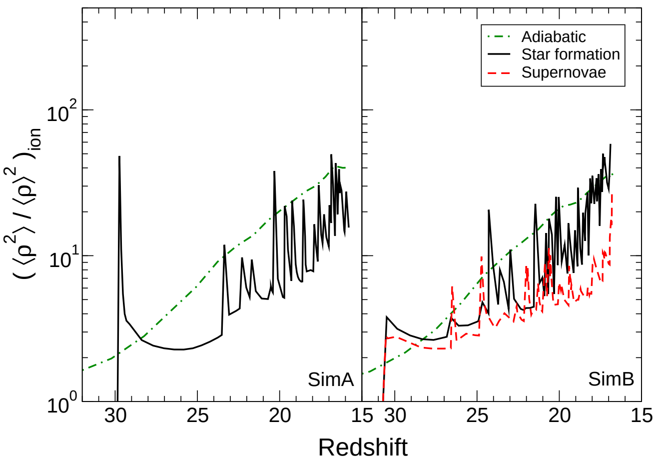

FIG. 10.— Clumping factor in ionized regions with $f_e > 10^{-3}$ for SimA (left) and SimB (right). The line styles are the same as in Figure 9.

4.3. *Clumping Factor Evolution*

Volume averaged recombination rates in an inhomogeneous IGM scale with the clumping factor $C = \langle\rho^2\rangle/\langle\rho\rangle^2$, where the angled brackets denote volume averaged quantities. The recombination rate for hydrogen, e.g., is simply

$$\left(\frac{dn_{\rm HII}}{dt}\right)_{\rm rec} = C k_{\rm rec} f_e \bar{\rho}_b (1+z)^3, \qquad (4)$$

where $k_{\rm rec}$ is the case B recombination rate for hydrogen at $T \approx 10^4$ K. Both the increased recombinations in overdense regions and photon escape fractions lower than unity result in the high number of UV photons needed for one effective ionization that we see in our simulations.

Figure 9 compares the clumping factor in the adiabatic, cooling only, star formation, and supernovae calculations. Since we resolve the local Jeans length by at least 4 cells in all simulations, the clumping factor is not underestimated, given our assumptions about gas cooling in each model. The RT and SN calculations capture the full evolution of the clumping factor since gas can fully condense by H_2 cooling in the pristine gas, accurately following the small-scale structure at low metallicities and high redshifts.

The clumping factor in the adiabatic case smoothly increases to $\sim$40 at $z = 17$ from unity at $z > 30$ because of the increase in number density of halos with masses above the cosmological Jeans mass. The cooling run only deviates from the adiabatic case when the most massive halo can start cooling by Lyα cooling, and the center begins a free-fall collapse, which causes the rapid increase in C. The clumping factor in the star formation only simulations become larger than the other simulations as several halos start to condense by H_2 cooling. The clumping decreases as these central concentrations are disbanded by stellar radiation. The combination of collapsing halos and stellar radiation generates fluctuations in the clumping factor around twice the value in the adiabatic case. SN explosions disperse gas more effectively than radiative feedback alone in larger halos and can have a bigger impact on the clumping factor. At redshift 20, the three stars and their SNe energy in the most massive halo destroy the surrounding baryonic structures and reduce the clumping back to the values seen in non-radiative cases. It marginally becomes larger at $z = 17$ but another SN lowers it again.

We show the clumping factor $C_{\rm ion}$ in ionized regions above $f_e > 10^{-3}$ in Figure 10. It fluctuates around half of the values found in adiabatic simulations. When an H II is still confined within its parent halo, the ionized material is still at high densities that causes the spikes in $C_{\rm ion}$. As the shock wave caused by the stellar radiation propagates into the IGM, baryon expulsion and photo-evaporation of small gas clumps in the H II regions cause $C_{\rm ion}$ to decrease. This repeats as star formation ensues and causes the fluctuations in $C_{\rm ion}$.

4.4. *Kinetic Energy Feedback*

SN explosion energy and kinetic energy generated in D-type I-front play a key role in star formation in low-mass halos, which are easily affected due to their shallow potential well (e.g. Dekel & Silk 1986; Haehnelt 1995; Bromm & Loeb 2003; Whalen et al. 2004; Kitayama et al. 2004; Kitayama & Yoshida 2005). The kinetic energy created by SNe is sufficient to expel the gas from these low-mass halos. For example, the binding energy of a $10^6 M_\odot$ halo is only 2.8×10^{50} erg at $z = 20$, which is two orders of magnitude smaller than a typical energy output of a pair instability SN (Heger & Woosley 2002). For a $T_{\rm vir} > 10^4$ K halo at the same redshift, it is 9.4×10^{52} erg. With our chosen stellar mass of 170 $M_\odot$, it takes 3 – 4 SNe to overcome this potential energy.

The shock wave created by the D-type I-front travels at a velocity $v_s = 25 - 35$ km s^{-1} for density gradients (i.e. $\rho(r) \propto r^{-w}$) with slopes between 1.5 and 2.25 (Shu et al. 2002; Whalen et al. 2004; Kitayama et al. 2004). This velocity is the escape velocity for halos with masses greater than $3 \times 10^8 M_\odot$ at $z = 15$, which is an order of magnitude greater than the most massive halos studied here. However less massive halos can contain these I-fronts because pressure forces slow the I-front after the star dies.

Using the position of the shock wave when the star dies (eq. 6) and energy arguments, we can estimate the critical halo mass where the material in the D-type I-

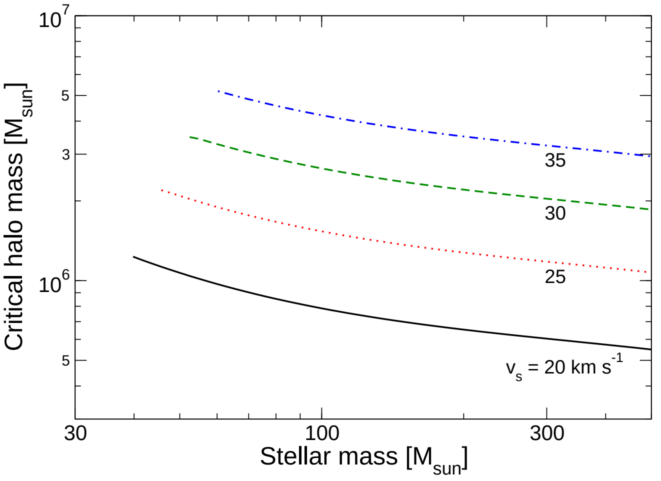

FIG. 11.— Maximum halo mass in which a D-type ionization front can create outflows as a function of primordial stellar mass for shock velocities v_s of 20, 25, 30, and 35 km s^{-1}. Here the fraction η of mass contained in the shell is 0.9.

front can escape from the halo by comparing the binding energy E_b of the halo and kinetic energy in the shell. For most massive stars, the shock wave never reaches the final Strömgren radius,

$$R_{\rm str} = 150 \left(\frac{\dot{N}_{\rm HI}}{10^{50} {\rm ph\ s}^{-1}} \right)^{1/3} \left(\frac{n_f}{1 \ {\rm cm}^{-3}} \right)^{-2/3} \ {\rm pc}, \quad (5)$$

before the star dies. Here $\dot{N}_{\rm HI}$ is the ionizing photon rate of the star, and n_f is the average number density of gas contained in this radius. After the lifetime of the star, the shock reaches a radius

$$R_s = 83 \left(\frac{v_s}{30 \ {\rm km\ s}^{-1}} \right) \left(\frac{t_\star}{2.7 {\rm Myr}} \right) \ {\rm pc}, \quad (6)$$

where $t_\star$ is the stellar lifetime (see also Kitayama et al. 2004). We can neglect isolated, lower mass (M $\lesssim 30 M_\odot$) Pop III stars whose shock wave reaches $R_{\rm str}$ within its lifetime. In this case, the I-front stops at $R_{\rm str}$, and the shock wave becomes a pressure wave that has no associated density contrast in the neutral medium (Shu 1992). Thus we can safely ignore these stars in this estimate.

Assume that the source is embedded in a single isothermal sphere. The mass contained in the shell is

$$M_{\rm sw} = \frac{(\Omega_b/\Omega_M) \, M_{\rm vir} \, R_s}{r_{\rm vir}} - V_s \rho_i \quad (7)$$

that is the mass enclosed in the radius R_s in an isothermal sphere, corrected for the warm, ionized medium behind the I-front. Here V_s is the volume contained in a sphere of radius R_s, and ρ_i is the gas density of the ionized medium, whose typical number density is 1 cm^{-3} for stellar feedback from a massive primordial star (Whalen et al. 2004; Kitayama et al. 2004; Yoshida et al. 2007a; Abel et al. 2007). For massive stars ($M_\star \gtrsim 30 M_\odot$), the mass of the central homogeneous medium is small (i.e. 10%) compared to the shell. We compensate for this interior mass by introducing the fraction η, so the shell mass is simply

$$M_{\rm sw} = \eta \, \frac{(\Omega_b/\Omega_M) \, M_{\rm vir} \, r_s}{r_{\rm vir}}. \quad (8)$$

For these outflows to escape from the halo, the kinetic energy contained in the shell must be larger than the binding energy, which is

$$\frac{1}{2} M_{\rm sw} v_s^2 \ > \ \frac{G M_{\rm vir}^2}{2 r_{\rm vir}}. \quad (9)$$

Using equations (6) and (8) in this condition, we obtain the maximum mass

$$M_{\rm max} \sim \frac{r_s \, v_s^2 \, \Omega_b}{G \, \Omega_M}$$

$$M_{\rm max} \sim 3.20 \times 10^6 \left(\frac{r_s}{100 {\rm pc}} \right) \left(\frac{v_s}{30 \ {\rm km\ s}^{-1}} \right)^2 \times \left(\frac{\eta}{0.9} \right) \left(\frac{\Omega_b/\Omega_M}{0.17} \right) M_\odot \quad (10)$$

of a halo where the material in the shock wave becomes unbound, expelling the majority of the gas from the halo.

In Figure 11, we use the stellar lifetimes and ionizing luminosities from Schaerer (2002) to calculate the critical halo mass for outflows for stellar masses $5 - 500 M_\odot$ and for shock velocities of 20, 25, 30, and 35 km s^{-1} with $\eta = 0.9$. For stellar masses smaller than $30 M_\odot$, the D-type I-front reaches the final Strömgren sphere and cannot expel any material from the host. Hence they are not plotted in this figure. For the more massive stars, the star dies before the D-type I-front can reach the Strömgren radius, thus being limited by $t_\star$. This maximum halo mass is in good agreement with our simulations as we see halos with masses greater than $5 \times 10^6 M_\odot$ retaining most of their gas in the star formation only cases. However in larger halos, stellar sources still generate champagne flows, but this material is still bound to the halo and returns in tens of million years.

4.5. *Thermal Energy*

Thermal feedback is yet another mechanism how Pop III stars leave their imprint on the universe. The initial heating of the IGM will continue and intensify from higher SFRs at lower redshifts (e.g. Hernquist & Springel 2003; Onken & Miralda-Escudé 2004). It is possible to constrain the reionization history by comparing temperatures in the Lyα forest to different reionization scenarios (Hui & Haiman 2003). Temperatures in the Lyα forest are approximately 20,000 K at $z = 3 - 5$ (Schaye et al. 2000; Zaldarriaga et al. 2001). Although our focus was not on redshifts below 15 due to the uncertainty of the transition to the first low-mass metal-enriched (Pop II) stars, we can utilize the thermal data in our radiation hydrodynamical simulations to infer the thermal history of the IGM at lower redshifts.

The excess energy from hydrogen ionizing photons over 13.6 eV photo-heat the gas in the H II region. The mean temperature within H II regions in our calculations is ~30,000 K. When the short lifetime of a Pop III star is over, the H II region cools mainly through Compton cooling off the cosmic microwave background. The same framework applies to SNe remnants as well. The timescale for Compton cooling is

$$t_C = 1.4 \times 10^7 \left(\frac{1+z}{20} \right)^{-4} f_e^{-1} \ {\rm yr}. \quad (11)$$

This process continues until the gas recombines, and Compton cooling is no longer efficient because of its

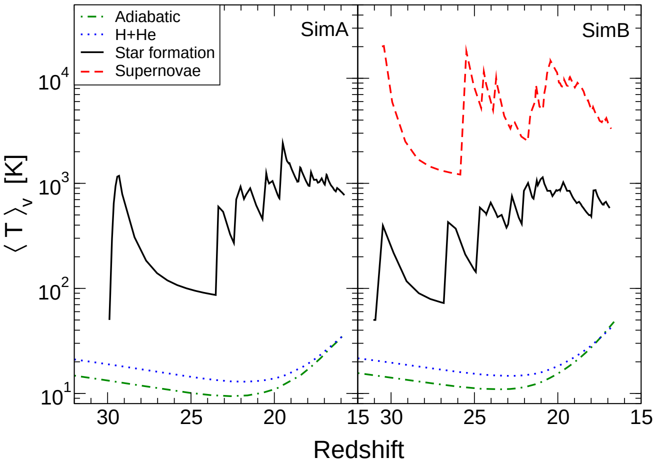

FIG. 12.— Evolution of the volume-averaged temperature in the inner 250 and 300 comoving kpc for Sim A (left) and Sim B (right), respectively. The simulations for the adiabatic (dot-dashed), cooling only (dotted), star formation only (solid), and supernovae (dashed) simulations are plotted.

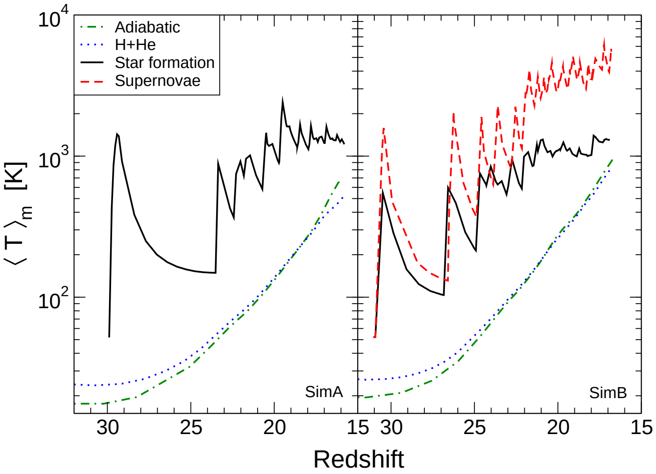

FIG. 13.— Same as Figure 12 but for the mass-averaged temperature.

dependence on electron fraction. Radiation preferentially propagates into the voids and leaves the adjacent filaments and its embedded halos virtually untouched. Hence we can restrict the importance of Compton cooling to the diffuse IGM since Compton cooling cools the gas to low temperatures without being impeded by recombinations that are proportional to n_e^2. This causes the relic H II region to cool to temperatures down to 300 K. The temperature evolution in our radiative calculations agrees with the analytic models of relic H II (Oh & Haiman 2003).

We plot the volume-averaged temperature $\langle T \rangle_{\rm v}$ and mass-averaged temperature $\langle T \rangle_{\rm m}$ in the volume where we allow star formation, i.e. the inner 250 (300) comoving kpc, in Figures 12 and 13. The first star in the calculations raises the volume averaged temperatures to 1200 (400) K. The mass-averaged temperatures are slightly higher at 1400 (550) K since the star has heated a larger fraction of mass, its host halo, when compared to the volume of the H II region. The supernovae calculations are even higher due to the hot SN bubble that has an initial temperature of 10^8 K. The high initial temperature causes the mass-averaged temperature in the SN simulations to spike when SNe occur to several times higher than the RT simulations. Afterwards the remnant cools from Compton and adiabatic processes as it expands to temperatures similar to the RT simulations.

Because photo-heating is confined to the H II regions, the trends seen in average temperatures follows the same behavior as the ionization fraction with the exception of the spikes associated with SNe. In the RT simulations, the volume-averaged temperature rises gradually from 500 K to 1000 K from redshifts 25 to 15. The mass-averaged temperature increases more than $\langle T \rangle_{\rm v}$ because of the photo-heating of the host halo and virial heating of the halos, which is the cause of the increase in the simulations without star formation. Without SNe, $\langle T \rangle_{\rm m}$ is only up to two times the temperatures in the no star formation runs. $\langle T \rangle_{\rm m}$ in the SN calculations exhibit a sharp transition to higher temperatures around 4000 K at $z = 21$, corresponding to the same episode with three successive stars forming and their SNe disrupting their $10^7 M_\odot$ host halo.

The photo-heating is better represented by the average temperature $\langle T \rangle_{\rm v}^{\rm ion}$ in ionized regions, which is plotted in Figure 14b. The first few stars heat the gas up to 20,000 K that then cool by adiabatic expansion and Compton cooling. When star formation occurs in several halos and the ionized filling fraction increases, the average temperature fluctuates around 6000 K because there are both active and relic H II in the simulation, causing $\langle T \rangle_{\rm v}^{\rm ion}$ to be lower than 20,000 K that happens during the formation of the first few H II regions. The increased temperatures cause the photo-evaporated and Jeans smoothing of the gas in the relic H II regions. We discuss these effects in the next section.

5. DISCUSSION

We have studied the details of massive metal-free star formation and its role in the start of cosmological reionization. We have treated star formation and radiation in a self-consistent manner, allowing for an accurate investigation of the evolution of cosmic structure under the influence of early Pop III stars. Stellar radiation from these stars provides thermal, dynamical, and ionizing feedback to the host halos and IGM. Although Pop III stars are not thought to provide the majority of ionizing photons needed for cosmological reionization, they play a key role in the early universe because early galaxies that form in these relic H II regions are significantly affected by Pop III feedback. Hence it is important to consider primordial stellar feedback while studying early galaxy formation. In this section, we compare our results to previous numerical simulations and semi-analytic models of reionization and then discuss any potential caveats of our methods and possible future directions of this line of research.

5.1. *Comparison to Previous Models*

5.1.1. *Filtering Mass*

One source of negative feedback is the suppression of gas accretion into potential wells when the IGM is preheated. The lower limit of the mass of a star forming

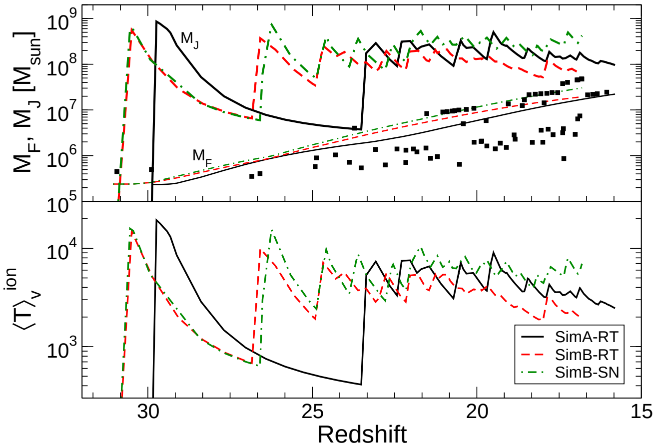

FIG. 14.— (a) The Jeans mass M_J and filtering mass M_F that can form bound objects. The squares denote the total mass of star forming halos in all three simulations. (b) Volume-averaged temperature in the ionized regions ($f_e > 10^{-3}$) that is used in computing the filtering mass.

halo is the Jeans filtering mass

$$M_F^{2/3}(a) = \frac{3}{a} \int_0^a da' M_J^{2/3}(a') \left[1 - \left(\frac{a'}{a} \right) \right], \qquad (12)$$

where a and M_J are the scale factor and time dependent Jeans mass in the H II region (Gnedin & Hui 1998; Gnedin 2000b). Additionally, the virial shocks are weakened if the accreting gas is preheated and will reduce the collisional ionization in halos with $T_{\rm vir} \gtrsim 10^4$ K. To illustrate the effect of Jeans smoothing, we take the large H II region of SimB-SN because it has the largest ionized filling fraction, which is constantly being heated after $z = 21$. Temperatures in this region fluctuates between 1,000 K and 30,000 K, depending on the proximity of the currently living stars. In Figure 14, we show the volume-averaged temperature and the resulting filtering mass of regions with an ionization fraction greater than 10^{-3} along with the total mass of star forming halos.

Gnedin (2000b) found the minimum mass of a star forming halo is better described by M_F instead of M_J. Our simulations are in excellent agreement for halos that are experiencing star formation after reincorporation of their previously expelled gas. The filtering mass is the appropriate choice for a minimum mass in this case as the halo forms from preheated gas. However for halos that have already assembled before they become embedded in a relic H II region, the appropriate minimum mass $M_{\rm min}$ is one that is regulated by the LW background (Machacek et al. 2001; Wise & Abel 2005) and photo-evaporation (e.g. Efstathiou 1992; Barkana & Loeb 1999; Haiman et al. 2001; Mesigner et al. 2006). This is evident in the multitude of star forming halos below M_F. With the exception of star formation induced by SN blast waves or I-fronts, this verifies the justification of using $M_{\rm min}$ and M_F for Pop III and galaxy formation, respectively, as a criterion for star forming halos in semi-analytic models.

5.1.2. *Star Formation Efficiency*

Semi-analytic models rely on a star formation efficiency $f_\star$, which is the fraction of collapsed gas that forms stars, to calculate quantities such as emissivities, chemical enrichment, and IGM temperatures. Low-mass halos that form a central star have $f_\star \sim 10^{-3}$ whose value originates from a single 100 $M_\odot$ star forming in a dark matter halo of mass 10^6 $M_\odot$ (Abel et al. 2002; Bromm et al. 2002; Yoshida et al. 2006). Pop II star forming halos are usually calibrated with star formation efficiencies from local dwarf and high-redshift starburst galaxies and are usually on the order of a few percent (e.g. Taylor et al. 1999; Gnedin 2000a).

This leads to the question: how efficient is star formation in these high-redshift halos while explicitly considering feedback? This is especially important when halos start to form multiple massive stars and when metallicities are not sufficient to induce Pop II star formation. The critical metallicity for a transition to Pop II is still unclear. Recently, Jappsen et al. (2007a) showed that metal line cooling is dynamically unimportant in diffuse gas until metallicities of 10^{-2} $Z_\odot$. On the other hand, dust that is produced in SNe can generate efficient cooling down in dense gas with $10^{-6}\,Z_\odot$ (Schneider et al. 2006). If the progenitors of the more massive halos did not result in a pair-instability SN, massive star formation can continue until it becomes sufficiently enriched. Hence our simulations can probe the efficiency of this scenario of massive metal-free star formation. It has also been suggested that the cosmological conditions that lead to the collapse of a metal-poor molecular cloud ($Z/Z_\odot \approx 10^{-3.5}$) may be more important than some critical metallicity in determining the initial mass function of a given stellar system (Jappsen et al. 2007b).

We calculate $f_\star$ with the ratio of the sum of the stellar masses to the total gas mass of unique star-forming halos. For example at the final redshift of 15.9 in SimA-RT, the most massive halo and its progenitors had hosted 11 stars and the gas mass of this halo is $1.8 \times 10^6 M_\odot$, which results in $f_\star = 6.1 \times 10^{-4}$ for this particular halo. Expanding this quantity to all star forming halos, $f_\star / 10^{-4} = 5.6, 6.7, 7.4$ for SimA-RT, SimB-RT, and SimB-SN, respectively. We note that our choice of $M_\star = 170 M_\odot$ in SimB-SN increases $f_\star$ by 70%. Our efficiencies are smaller than the isolated Pop III case because halos cannot form any stars once the first star expels the gas, and 40 – 75 million years must pass until star can form again when the gas is reincorporated into the halo.

By regarding the feedback created by Pop III stars and associated complexities during the assembly of these halos, the $f_\star$ values of $\sim 6 \times 10^{-4}$ that are explicitly determined from our radiation hydrodynamical simulations provide a more accurate estimate on the early star formation efficiencies.

5.1.3. *Intermittent & Anisotropic Sources*

Our treatment of star formation and feedback produces intermittent star formation, especially in low-mass halos. If one does not account for this, star formation rates might be overestimated in this phase of star formation. Kinetic energy feedback is the main cause of this behavior. As discussed in sections 3.2 and 4.4, shock waves created by D-type I-fronts and SN explosions expel most of the gas in halos with masses $\lesssim 10^7$ $M_\odot$. A period of quiescence follows these instances of star formation. Then stars are able to form after enough material has accreted back into the halo. Only when the halo becomes massive enough to retain most of the outflows and cool efficiently through Lyα and H$_2$ radiative processes, star formation

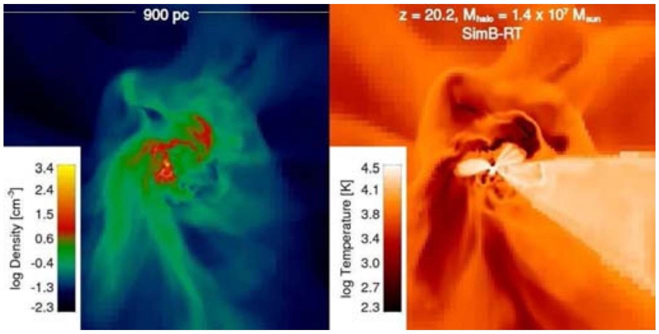

Fig. 15.— Density (left) and temperature (right) slices of an anisotropic H II region in the most massive halo of SimB-RT. The star has lived for 2.5 Myr out of its 2.7 Myr lifetime. The field of view is 900 proper parsecs.

becomes more regular with successive stars forming.

The central gas structures in the host halo are usually anisotropic as it is acquiring material through accretion along filaments and mergers. At scales smaller than 10 pc, the most optically thick regions produce shadows where the gas radially behind the dense clump is not photo-ionized or photo-heated by the source. This produces cometary and so-called elephant trunk structures that are also seen in local star forming regions and have been discussed in detail since Pottasch (1958). At a larger distance, the surrounding cosmic structure is composed of intersecting or adjacent filaments and satellite halos that breaks spherical symmetry. The filaments and nearby halos are optically thick and remain cool and thus the density structures are largely unchanged. The entropy of dense regions are not increased by stellar radiation and will feel little negative feedback from an entropy floor that only exists in the ionized IGM (cf. Oh & Haiman 2003). Ray-tracing allows for accurate tracking of I-fronts in this inhomogeneous medium. Radiation propagates through the least optically thick path and generates champagne flows that have been studied extensively in the context of present day star formation (e.g. Franco et al. 1990; Churchwell 2002; Shu et al. 2002; Arthur & Hoare 2006). In the context of massive primordial stars, these champagne flows spread into the voids and are impeded by the inflowing filaments. The resulting H II regions have "butterfly" morphologies (Abel et al. 1999, 2007; Alvarez et al. 2006a; Mellema et al. 2006; Yoshida et al. 2007a). We also point out that sources embedded in relic H II largely maintain or increase the ionization fraction. Here the already low optical depth of the recently ionized medium (within a recombination time) allows the radiation to travel to greater distances than a halo embedded in a completely neutral IGM. The H II regions become increasingly anisotropic in higher mass halos. We show an example of the morphology of a H II region near the end of the star's lifetime in a dark matter halo with mass $1.4 \times 10^7 M_\odot$ in Figure 15.

5.2. *Potential Caveats and Future Directions*

Although we have simulated the first generations of stars with radiation hydrodynamic simulations, our methods have neglected some potentially important processes and made an assumption about the Pop III stellar masses.

One clear shortcoming of our simulations is the small volume and limited statistics of the objects studied here. However, it was our intention to focus on the effects of Pop III star formation on cosmological reionization and on the formation of an early dwarf galaxy instead of global statistics. We have verified even in a 2.5-σ peak that Pop III stars cannot fully reionize the universe, which verified previous conclusions that low-luminosity galaxies provide the majority of ionizing photons. Furthermore, it is beneficial to study Pop III stellar feedback because it regulates the nature of star formation in these galaxies that form from pre-heated material. Further radiation hydrodynamics simulations of primordial star and galaxy formation with larger volumes while still resolving the first star forming halos of mass $\sim 3 \times 10^5 M_\odot$ will improve the statistics of early star formation, especially in more typical overdensities, i.e. 1-σ peaks, some of which could survive to become dwarf spheroidal galaxies at $z = 0$.

In this work, we treated the LW radiation field as optically thin, but in reality, H_2 produces a non-zero optical depth above column densities of 10^{14} cm^{-2} (Draine & Bertoldi 1996). Conversely, Doppler shifts of the LW lines arising from large velocity anisotropies and gradient may render H_2 self-shielding unimportant up to column densities of $10^{20} - 10^{21}$ cm^{-2} (Glover & Brand 2001). If self-shielding is important, it will lead to increased star formation in low-mass halos even when a nearby source is shining. Moreover, H_2 production can also be catalyzed ahead of I-fronts (Ricotti et al. 2001; Ahn & Shapiro 2007). In these halos, LW radiation will be absorbed before it can dissociate the central H_2 core. On the same topic, we neglect any type of soft UV or LW background that is created by sources that are cosmologically nearby ($\Delta z/z \sim 0.1$). A soft UV background either creates positive or negative feedback, depending on its strength (Mesigner et al. 2006), and a LW background increases the minimum halo mass of a star-forming halo (Machacek et al. 2001; Yoshida et al. 2003; O'Shea & Norman 2007; Wise & Abel 2007b). However in our calculations, the lack of self-shielding, which suppresses star formation in low-mass halos, and the neglect of a LW background, which allows star formation in these halos, may partially cancel each other. Hence one may expect no significant deviations in the SFRs and reionization history if one treats these processes explicitly.

To address the incident radiation and the resulting UV background from more rare density fluctuations outside of our simulation volume, it will be useful to bridge the gap between the start of reionization on Mpc scales to larger scale (10 − 100 Mpc) simulations of reionization, such as the work of Sokasian et al. (2003), Iliev et al. (2006), Zahn et al. (2007), and Kohler et al. (2007). Radiation characteristics from a volume that has similar overdensities as our Mpc-scale simulations can be sampled from such larger volumes to create a radiation background that inflicts the structures in our Mpc scale simulations. Inversely, perhaps the small-scale evolution of the clumping factor, filtering mass, and average temperature and ionization states can be used to create an accurate subgrid model in large volume reionization simulations.

Another potential caveat is the continued use of primordial gas chemistry in metal enriched regions in the SN runs. Our simulations with SNe give excellent initial conditions to self-consistently treating the transition to low-mass star formation. In future work, we plan to introduce metal-line and dust cooling models (e.g. from Glover & Jappsen 2007; Smith & Sigurdsson 2007) to study this transition.

The one main assumption about Pop III stars in our calculations is the fixed, user-defined stellar mass. The initial mass function (IMF) of these stars is largely unknown, therefore we did not want to introduce an uncertainty by choosing a fiducial IMF. It is possible to calculate a rough estimate of the stellar mass by comparing the accretion rates and Kelvin-Helmholtz time of the contracting molecular cloud (Abel et al. 2002; O'Shea et al. 2005). Protostellar models of primordial stars have also shown that the zero-age main sequence (ZAMS) is reached at 100 $M_\odot$ for typical accretion histories after the star halts its adiabatic contraction (Omukai & Palla 2003; Yoshida et al. 2006). Furthermore, we have neglected HD cooling, which may become important in halos embedded in relic H II regions and result in lower mass ($\sim$30$M_\odot$) metal-free stars (O'Shea et al. 2005; Greif & Bromm 2006; Yoshida et al. 2007b). Based on accretion histories of star forming halos, one can estimate the ZAMS stellar mass for each halo and create a more self-consistent and ab initio treatment of Pop III star formation and feedback.

6. SUMMARY

We conducted three radiation hydrodynamical, adaptive mesh refinement simulations that supplement our previous cosmological simulations that focused on the hydrodynamics and cooling during early galaxy formation. These new simulations concentrated on the formation and feedback of massive, metal-free stars. We used adaptive ray tracing to accurately track the resulting H II regions and followed the evolution of the photo-ionized and photo-heated IGM. We also explored on the details of early star formation in these simulations. Theories of early galaxy formation and reionization and large scale reionization simulations can benefit from the useful quantities and characteristics of the high redshift universe, such as SFR and IGM temperatures and ionization states, calculated in our simulations. The key results from this work are listed below.

1. SFRs increase from 5×10^{-4} at redshift 30 to 6×10^{-3} M$_\odot$ yr^{-1} Mpc^{-3} at redshift 20 in our simulations. Afterwards the SFR begins to have a bursting nature in halos more massive than $10^7 M_\odot$ and fluctuates around 10^{-2} M$_\odot$ yr^{-1} Mpc^{-3}. These rates are larger than the ones calculated in Hernquist & Springel (2003) because our simulation volume samples a highly biased region that contains a 2.5-σ density fluctuation. The associated emissivity from these stars increase from 1 to $\sim$100 ionizing photons per baryon per Hubble time between redshifts 15 and 30.
2. In order to provide a comparison to semi-analytic models, we calculate the star formation efficiency to be $\sim 6\times10^{-4}$ averaged over all redshifts and the simulation volume. For Pop III star formation, this is a factor of two lower than stars that are not affected by feedback (Abel et al. 2002; Bromm et al. 2002; Yoshida et al. 2006; O'Shea & Norman 2007).
3. Shock waves created by D-type I-fronts expel most of the gas in the host halos below $\sim 5\times10^6 M_\odot$. Above this mass, significant outflows that are still bound to the halo are generated. This feedback creates a dynamical picture of early structure formation, where star formation is suppressed in halos because of this baryon depletion, which is more effective than UV heating or the radiative dissociation of H$_2$.
4. We see three instances of induced star formation in halos with masses $\sim 3\times10^6 M_\odot$. Here a star forms as a SN blast wave overtakes an overdensity created by an ionization front instability. H$_2$ formation is catalyzed by additional free electrons in the relic H II region and in the SN blast wave (Ferrara 1998).
5. As star formation occurs regularly in the simulation after redshift 25, four (six) ionizing photons are needed per sustained hydrogen ionization. As the most massive halo becomes larger than $\sim 10^7 M_\odot$ in the simulations without SNe, H II regions become trapped and ionizing radiation only escapes into the IGM in small solid angles. Hence the number of photons per effective ionization increases to 15 (50). In SimB-SN, stellar radiation from induced star formation have an escape fraction of nearly unity, which occur four times in the calculation. This allows the IGM to remain ionized at a volume fraction 3 times higher than without SNe. Similarly, the ionizing photon to ionization ratio also stays elevated at 10:1 instead of decreasing in the calculations with star formation only.
6. Our simulations that include star formation and H$_2$ formation capture the entire evolution of the clumping factor that is used in semi-analytic models to calculate the effective enhancement of recombinations in the IGM. We showed that clumping factors in the ionized medium fluctuate around the half of the values found in adiabatic simulations. They evolve from unity at high redshifts and steadily increase to $\sim$10 and 40 with and without SNe, respectively. Photo-evaporation from stellar feedback causes the fluctuations of the clumping factor.
7. We calculated the Jeans filtering mass with the volume-averaged temperature only in fully and partially ionized regions, which yields a better estimate than the temperature averaged over both ionized and neutral regions. The filtering mass depends on the thermal history of the IGM, which mainly cools through Compton cooling. It increases by two orders of magnitude to $\sim 3\times10^7 M_\odot$ at $z \sim 15$. It describes the minimum mass a halo requires to collapse after hosting a Pop III star. For halos forming their first star, the minimum halo mass is regulated by the LW background (Machacek et al. 2001) and photo-evaporation (e.g. Haiman et al. 2001).

Pop III stellar feedback plays a key role in early star formation and the beginning of cosmological reionization. The shallow potential wells of their host halos only amplify their radiative feedback. Our understanding of the formation of the oldest galaxies and the characteristics of isolated dwarf galaxies may benefit from including the earliest stars and their feedback in galaxy formation models. Although these massive stars only partially reionized the universe, their feedback on the IGM and galaxies is crucial to include since it affects the characteristics of low-mass galaxies that are thought to be primarily responsible for cosmological reionization. Harnessing observational clues about reionization, observations of local dwarf spheroidal galaxies, and numerical simulations that accurately handle star formation and feedback may provide great insight on the formation of the first galaxies, their properties, and how they completed cosmological reionization.

This work was supported by NSF CAREER award AST-0239709 from the National Science Foundation and partially supported in part by the National Science Foundation under Grant No. PHY05-51164. J. H. W. thanks Renyue Cen for helpful discussions. We benefited from fruitful conversations with Marcelo Alvarez. We are grateful for the continuous support from the computational team at SLAC. We benefited the hospitality of KITP at UC Santa Barbara, where this work was completed. We performed these calculations on 16 processors of a SGI Altix 3700 Bx2 at KIPAC at Stanford University.

REFERENCES

Abel, T., Anninos, P., Zhang, Y., & Norman, M. L. 1997, New Astronomy, 2, 181
Abel, T., Anninos, P., Norman, M. L., & Zhang, Y. 1998, ApJ, 508, 518
Abel, T., Norman, M. L., & Madau, P. 1999, ApJ, 523, 66
Abel, T., Bryan, G. L., & Norman, M. L. 2000, ApJ, 540, 39
Abel, T., Bryan, G. L., & Norman, M. L. 2002, Science, 295, 93
Abel, T. & Wandelt, B. D. 2002, MNRAS, 330, L53
Abel, T., Wise, J. H., & Bryan, G. L. 2007, ApJ, 659, L87
Ahn, K., & Shapiro, P. R. 2007, MNRAS, 375, 881
Alvarez, M. A., Bromm, V., & Shapiro, P. R. 2006a, ApJ, 639, 621
Alvarez, M. A., Shapiro, P. R., Ahn, K., & Iliev, I. T. 2006, ApJ, 644, L101
Anninos, P., Zhang, Y., Abel, T., & Norman, M. L. 1997, New Astronomy, 2, 209
Arthur, S. J., & Hoare, M. G. 2006, ApJS, 165, 283
Barkana, R., & Loeb, A. 1999, ApJ, 523, 54
Bouwens, R. J., et al. 2004, ApJ, 606, L25
Bowman, J. D., et al. 2007, AJ, 133, 1505
Bromm, V., Coppi, P. S., & Larson, R. B. 2002, ApJ, 564, 23
Bromm, V. & Loeb, A, 2003, ApJ, 596, 34
Bryan, G. L. & Norman, M. L. 1997, in Computational Astrophysics, eds. D. A. Clarke and M. Fall, ASP Conference #123
Bryan, G. L. & Norman, M. L. 1999, in Workshop on Structured Adaptive Mesh Refinement Grid Methods, IMA Volumes in Mathematics No. 117, ed. N. Chrisochoides, p. 165
Cen, R., & Ostriker, J. P. 1992, ApJ, 399, L113
Churchwell, E. 2002, ARA&A, 40, 27
Cooray, A., et al. 2007, ApJ, 659, L91
Dekel, A., & Rees, M. J. 1987, Nature, 326, 455
Dekel, A., & Silk, J. 1986, ApJ, 303, 39
Draine, B. T., & Bertoldi, F. 1996, ApJ, 468, 269
Efstathiou, G. 1992, MNRAS, 256, 43P
Eisenstein, D. J. & Hut, P. 1998, ApJ, 498, 137
Eyles, L. P., Bunker, A. J., Ellis, R. S., Lacy, M., Stanway, E. R., Stark, D. P., & Chiu, K. 2006, MNRAS, 1348
Fan, X., Fan, X., et al. 2006, AJ, 132, 117
Ferrara, A. 1998, ApJ, 499, L17
Franco, J., Tenorio-Tagle, G., & Bodenheimer, P. 1990, ApJ, 349, 126
Gardner, J. P., et al. 2006, Space Science Reviews, 123, 485
Gehrels, N., et al. 2004, ApJ, 611, 1005
Glover, S. C. O., & Brand, P. W. J. L. 2001, MNRAS, 321, 385
Glover, S. C. O., & Jappsen, A.-K., 2007, ApJ, 666, 1
Gnedin, N. Y. 2000a, ApJ, 535, L75
Gnedin, N. Y. 2000b, ApJ, 542, 535
Gnedin, N. Y., & Hui, L. 1998, MNRAS, 296, 44
Greif, T. H. & Bromm, V. 2006, MNRAS, 373, 128
Haehnelt, M. G. 1995, MNRAS, 273, 249
Haiman, Z., Abel, T., & Madau, P. 2001, ApJ, 551, 599
Haiman, Z., Abel, T., & Rees, M. J. 2000, ApJ, 534, 11
Haiman, Z., Thoul, A. A., & Loeb, A. 1996, ApJ, 464, 523
Heger, A. & Woosley, S. E. 2002, ApJ, 567, 532
Hernquist, L., & Springel, V. 2003, MNRAS, 341, 1253
Hui, L., & Haiman, Z. 2003, ApJ, 596, 9
Iliev, I. T., Mellema, G., Pen, U.-L., Merz, H., Shapiro, P. R., & Alvarez, M. A. 2006, MNRAS, 369, 1625
Jappsen, A.-K., Glover, S. C. O., Klessen, R. S., & Mac Low, M.-M. 2007, ApJ, 660, 1332
Jappsen, A.-K., Klessen, R. S., Glover, S. C. O., & Mac Low, M.-M. 2007, ApJ, *submitted*, `arXiv:0709.3530`
Johnson, J. L., Greif, T. H., & Bromm, V. 2007, ApJ, 665, 85
Kashlinsky, A., Arendt, R. G., Mather, J., & Moseley, S. H. 2007, ApJ, 654, L1
Kitayama, T., Yoshida, N., Susa, H., & Umemura, M. 2004, ApJ, 613, 631
Kitayama, T., & Yoshida, N. 2005, ApJ, 630, 675
Kohler, K., Gnedin, N. Y., & Hamilton, A. J. S. 2007, ApJ, 657, 15
Machacek, M. E., Bryan, G. L., & Abel, T. 2001, ApJ, 548, 509
Madau, P., Ferguson, H. C., Dickinson, M. E., Giavalisco, M., Steidel, C. C., & Fruchter, A. 1996, MNRAS, 283, 1388
Mellema, G., Iliev, I. T., Alvarez, M. A., & Shapiro, P. R. 2006, New Astronomy, 11, 374
Mesinger, A., Bryan, G. L., & Haiman, Z. 2006, ApJ, 648, 835
Nagakura, T., & Omukai, K. 2005, MNRAS, 364, 1378
O'Shea, B. W., Abel, T., Whalen, D., & Norman, M. L. 2005, ApJ, 628, L5
O'Shea, B. W., & Norman, M. L. 2007, ApJ, 654, 66
Oh, S. P., & Haiman, Z. 2003, MNRAS, 346, 456
Onken, C. A., & Miralda-Escudé, J. 2004, ApJ, 610, 1
Omukai, K., & Palla, F. 2003, ApJ, 589, 677
Ostriker, J. P., & McKee, C. F. 1988, Reviews of Modern Physics, 60, 1
Page, L., et al. 2007, ApJS, 170, 335
Pottasch, S. R. 1958, Reviews of Modern Physics, 30, 1053
Press, W. H. & Schechter, P. 1974, ApJ, 187, 425
Ricotti, M., Gnedin, N. Y., & Shull, J. M. 2001, ApJ, 560, 580
Ricotti, M., Gnedin, N. Y., & Shull, J. M. 2002a, ApJ, 575, 33
Ricotti, M., Gnedin, N. Y., & Shull, J. M. 2002b, ApJ, 575, 49
Rottgering, H. J. A., et al. 2006, ArXiv Astrophysics e-prints, arXiv:astro-ph/0610596
Schaerer, D. 2002, A&A, 382, 28
Schaye, J., Theuns, T., Rauch, M., Efstathiou, G., & Sargent, W. L. W. 2000, MNRAS, 318, 817
Schilizzi, R. T. 2004, Proc. SPIE, 5489, 62
Schneider, R., Omukai, K., Inoue, A. K., & Ferrara, A. 2006, MNRAS, 369, 1437
Sedov, L. I. 1959, Similarity and Dimensional Methods in Mechanics, New York: Academic Press, 1959
Shapiro, P. R. 1986, PASP, 98, 1014
Sheth, R. K. & Tormen, G. 2002, MNRAS, 329, 61
Shu, F. H. 1992, *Physics of Astrophysics, Vol. II*, (Sausalito: University Science Books)
Shu, F. H., Lizano, S., Galli, D., Cantó, J., & Laughlin, G. 2002, ApJ, 580, 969
Smith, B. D., Sigurdsson, S., & Abel T. 2007, MNRAS, *submitted*, `arXiv:0706.0754`
Sokasian, A., Abel, T., Hernquist, L., & Springel, V. 2003, MNRAS, 344, 607
Spergel, D. N., et al. 2003, ApJS, 148, 175
Spergel, D. N., et al. 2007, ApJS, 170, 377
Swarup, G., Ananthakrishnan, S., Kapahi, V. K., Rao, A. P., Subrahmanya, C. R., & Kulkarni, V. K. 1991, Current Science, 60, 95
Taylor, C. L., Hüttemeister, S., Klein, U., & Greve, A. 1999, A&A, 349, 424
Tegmark, M., Silk, J., Rees, M. J., Blanchard, A., Abel, T., & Palla, F. 1997, ApJ, 474, 1
Thompson, R. I., Eisenstein, D., Fan, X., Rieke, M., & Kennicutt, R. C. 2007, ApJ, 666, 658
Whalen, D., Abel, T., & Norman, M. L. 2004, ApJ, 610, 14
Whalen, D., & Norman, M. L. 2007a, ApJ, *accepted*, `astro-ph/0703463`
Whalen, D., & Norman, M. L. 2007b, ApJ, *submitted*, `arXiv:0708.2444`
Wilson, T. L., Beasley, A. J., & Wootten, H. A. 2005, ASP Conf. Ser. 344: The Cool Universe: Observing Cosmic Dawn, 344, 232
Wise, J. H., & Abel, T. 2005, ApJ, 629, 615
Wise, J. H., & Abel, T. 2007a, ApJ, 665, 899
Wise, J. H., & Abel, T. 2007b, ApJ, *accepted*, `arXiv:0707.2059`
Wise, J. H., & Abel, T. 2007c, ApJ, *submitted*, `arXiv:0710.3160`
Yoshida, N., Abel, T., Hernquist, L., & Sugiyama, N. 2003, ApJ, 592, 645
Yoshida, N., Oh, S. P., Kitayama, T., & Hernquist, L. 2007a, ApJ, 663, 687
Yoshida, N., Omukai, K., & Hernquist, L. 2007b, ApJ, 667, L117
Yoshida, N., Omukai, K., Hernquist, L., & Abel, T. 2006, ApJ, 652, 6

Zahn, O., Lidz, A., McQuinn, M., Dutta, S., Hernquist, L., Zaldarriaga, M., & Furlanetto, S. R. 2007, ApJ, 654, 12
Zaldarriaga, M., Hui, L., & Tegmark, M. 2001, ApJ, 557, 519